ORIGINAL PAPER

Effect of collagen damage induced by heat treatment on the mixed-mode fracture behavior of bovine cortical bone under elevated loading rates

Tanner Snow · William Woolley · Robert M. Metcalf · James Rosenberg · Claire Acevedo · Owen T. Kingstedt

Abstract The fracture resistance of bone has been attributed to a competition of sub-micron lengthscale intrinsic mechanisms, including plasticity conferred by collagen stretching and intermolecular sliding and much larger lengthscale extrinsic mechanisms such as crack deflection and bridging. In this study, the contribution of intrinsic toughening mechanisms on the dynamic fracture behavior of bovine cortical bone is investigated. Single edge notched cortical bone specimens were extracted from the mid-diaphysis of a bovine femur with dimensions in accordance with ASTM E399. Four specimen groups are studied, a control group, and groups subjected to two-hour heat treatments of 130 °C, 160 °C and 190 °C, respectively. Using a trypsin-hydroxyproline assay to determine the percent of denatured collagen achieved by each heat treatment, it is shown that the 160 °C and 190 °C groups have accumulated substantial collagen network damage compared to the 130 °C and control groups. Three-point bend drop tower experiments with impact velocities of 1.6 m/s. The selected impact velocity results in a nominal stress intensity factor rate of $\dot{K} = 1.5 \times 10^5 MPa\ m^{1/2}/s$. Specimen's speckled surfaces were imaged at 500,000 fps during deformation and post-processed using digital image correlation to determine the in-plane displacement fields. Using an orthotropic material linear elastic fracture mechanics formulation and over-deterministic least-squares analysis, the critical mode-I and mode-II stress intensity factors (i.e., fracture initiation toughness) were determined immediately proceeding fracture. As the heat treatment temperature increases (and the damaged collagen content increases), a weak but decreasing trend in fracture toughness was observed. Of particular note, for the 160 °C and 190 °C heat treatments, it was observed that the mode-II fracture initiation toughness is larger than the mode-I fracture initiation toughness. Regardless of the heat treatment condition, the mode-II fracture initiation toughness was comparatively less affected. For the specific case of Haversian bovine cortical bone whose collagen network has been denatured using heat treatment, a trend is observed pointing to collagen primarily conferring mode-I fracture initiation toughness, opposed to mode-II fracture initiation toughness, for the transverse fracture orientation.

1 Introduction

The mechanical behavior and governing mechanisms of bone are of significant scientific interest (Weiner

T. Snow · W. Woolley · R. M. Metcalf · J. Rosenberg ·
C. Acevedo · O. T. Kingstedt (✉)
Department of Mechanical Engineering, University of
Utah, Salt Lake City, UT 84112, USA
e-mail: o.kingstedt@utah.edu

C. Acevedo
Department of Biomedical Engineering, University of Utah, Salt
Lake City, UT 84112, USA

et al. 1999; Liu et al. 2000; Reilly and Currey 2000). Many studies, have examined the role of bone microstructure on the mechanical properties and fracture behavior of bone at quasi-static loading rates (e.g., Nalla et al. 2003, 2004; Yeni and Norman 2000; Silva and Gibson 1997; Acevedo et al. 2018). In order to advance understanding of the role of toughening mechanisms activated in response to a single catastrophic event causing bone fracture, such as a fall or impact event, there is a need to quantitatively assess the fracture behavior of bone under elevated loading rates. Furthermore, there is a need to determine if fracture toughening mechanisms observed under quasi-static loading regimes are active at elevated loading rates and to what extent they influence fracture behavior. Work by multiple groups has been conducted to assess the rate-dependent mechanical and fracture behavior of bone. Hansen et al. (2008) examined the role of strain-rate on the tensile behavior of human cortical bone. They found yield stress, failure stress and strain at failure to decrease for strain rates above $\dot{\varepsilon} > 1s^{-1}$. Additionally, specimens subjected to higher loading rates behaved in a more brittle fashion indicating a change in toughening mechanism behavior. Post-test examination of mechanism activity found microcracking to be inversely related to strain rate based on the observation that microcracking was more prevalent in low strain rate experiments (Zioupos et al. 2008). Shannahan et al. (2015) investigated the rate-dependent fracture behavior of human cortical bone at quasi-static, intermediate, and dynamic fracture rates and found isotropic material assumptions to underestimate fracture toughness at quasi-static and intermediate loading rates, but an over estimation for dynamic rates. Similarly, Sanborn et al. (2016) studied the rate-dependent fracture toughness of human cortical bone finding an increase in fracture toughness when comparing quasi-static and intermediate rate fracture toughness rates and a slight decrease in fracture toughness when comparing intermediate and dynamic fracture toughness rates. Kulin et al. (2011) examined the effect of loading rate on equine femur reporting fracture toughness to decrease when comparing quasi-static experiments to dynamic experiments. The efforts of Zimmermann et al. (2014) observed that in response to high-strain rate loading cracks were able to penetrate through osteons instead of deflecting along osteon cement lines. As will be discussed below, crack deflection is a predominant fracture toughening mechanism in cortical bone. Additionally, there was a progressive reduction in plasticity with increasing strain rate indicating a change in mechanism activity as a function of loading rate (Zimmermann et al. 2014). Zhai et al. (2019) studied the role of loading rate on cortical and trabecular porcine bone. With respect to cortical bone, they found the incipient crack propagation to be dependent on the intrinsic cortical bone microstructure regardless of loading condition and fracture toughness to decrease with increasing stress intensity rate ($\dot{K}$). In summary, fracture toughening mechanisms have been shown to change with loading rate.However, there is some disagreement on whether the fracture toughness of bovine cortical bone, when subjected to elevated loading rates, increases (e.g., Tanabe et al. 1998) or decreases (e.g., Adharapurapu et al. 2006) when compared to quasi-static fracture toughness values.

The goal of the presented study was to assess the critical mode-I and mode-II stress intensity factors (SIFs) at fracture initiation (i.e., fracture initiation toughness) at intermediate loading rates for healthy bovine cortical bone and quality impaired cortical bone whose collagen network has been degraded by heat treatment denaturation.

1.1 Bone microstructure and composition

The mechanical performance of bone, an anisotropic biocomposite, is governed by its hierarchical microstructure, which has distinct features at multiple length-scales. The hierarchical structure of bone has been presented in detail by Weiner and Daniel Wagner (1998) and Hillier and Bell (2007) and will only be summarized in the following. Cortical bone can be classified into three types: plexiform, Haversian (or osteonal) and interstitial. Plexiform bone has a lamellar structure perforated by blood vessels. Its sandwich-like structure is comprised of alternating layers of woven and lamellar bone tissue with thicknesses on the order of 70 ± 20 μm and 50 ± 10 μm respectively (Conward and Samuel 2016). Woven bone tissue is laid down quickly and consists of a poorly organized arrangement of collagen fibers surrounding blood vessels and nerves (Schultz 2001; Currey 2003). Lamellar bone tissue is laid down much more slowly and consists of well-organized parallel layers of collagen fibers and mineral phases (Sommerfeldt and Rubin 2001; Currey 2006). Plexiform bone is frequently observed in the long bones (e.g., femur) of large fast growing mammals including pigs,

cows, sheep, horse and water buffalo (Hillier and Bell 2007). The microstructure of Haversian bone is dominated by 200-300 μm diameter cylindrical osteons oriented parallel to the longitudinal direction. The osteons have 50-90 μm diameter central vascular channels (i.e., Haversian canals) surrounded by multiple layers of lamellar bone and an outer layer commonly referred to as cement lines that are brittle, minearalized, and mechanically weak. Haversian cortical bone is commonly found in the long bones of humans. Lastly, interstitial cortical bone fills the space between osteons and is comprised of remnants of the remodeling process (Manilay et al. 2013). The varying hierarchical structure of cortical bone presents a significant challenge in understanding the mechanisms governing fracture behavior. Therefore, it is of scientific interest to isolate the contributions of individual constituents of the hierarchical structure on cortical bone's mechanical and fracture properties.

Among the microstructural features of interest, the current study attempts to isolate the role of the collagen network quality on fracture behavior of bovine cortical bone exhibiting a Haversian dominated microstructure. Collagen network alteration has been previously shown to impact bone's post-yield mechanical properties in multiple mammalian species. Jepsen et al. investigated the impact of type-I collagen mutation in mice femur and found a significant reduction (61%) in the post-yield deflection compared to control specimens (Jepsen et al. 1996, 1997). Oxlund et al. studied the effect of reduced collagen cross-linking in rats on the long bone deflection at fracture, bending stress, and Young's modulus and found more than 20% reduction across all properties examined (Hans Oxlund et al. 1995). Wang et al. examined the effect of collagen denaturation achieved using heat treatments on human cadaver femurs. They found reductions in the yield strength, ultimate strength, and work of fracture for all heat treatment temperatures above 150 °C (Wang et al. 2000); the temperature at which mineralized collagen is denatured. Lee et al. found the stiffness and energy absorption to fracture to decrease with decreased collagen cross-linking in rabbit long bones (Lees et al. 1994). Todoh et al. examined the bending and impact properties of bovine cortical bone. Bending strength and fracture energy were both found to decrease with increasing collagen denaturation (Todoh et al. 2009). All of the aforementioned studies, with the exception of the impact study of Todoh et al. (2009) were limited

to quasi-static loading. Thus there is a gap in understanding the affect of collagen network degradation on the fracture resistance of bone at elevated loading rates.

1.2 Fracture resistance of bone

The fracture resistance of bone is generally considered to result from the competition of plastic deformation mechanisms ahead of the crack tip (i.e., intrinsic toughening mechanisms) and crack tip shielding mechanisms acting in the wake of the crack tip (i.e., extrinsic toughening mechanisms) (Launey et al. 2010). These intrinsic and extrinsic mechanisms are operative at separate lengthscales. Intrinsic mechanisms occur at the sub-micron lengthscale, while extrinsic mechanisms are active at scales greater than one micron. Intrinsic mechanisms are predominantly collagen-based and provide energy dissipation through plastic zone formation and failure around defects. Predominant intrinsic mechanisms include collagen molecule stretching and unwinding, intermolecular sliding, the breaking of bonds between collagen fiber arrays, and microcracking. The sliding of collagen molecules with each other and with the hydroxyapatite crystals provides a dissipative deformation process during plasticity, which increases bone fracture resistance (Buehler 2007). Fracture resistance is enhanced by the formation of local yield regions around defects (e.g., cracks), which enables microscale localized failure opposed to macroscale failure (Launey et al. 2010). Collagen fiber arrays are held together by an extracellular matrix (Fantner et al. 2005). It has been hypothesized that under tensile loading, the collagen fibril deforms uniaxially in the longitudinal direction sliding over each other while the extracellular matrix deforms in shear, acting like glue. The collagen fibril deforms by the subsequent breaking of sacrificial bonds at forces below those required to break the collagen molecule backbone. An alternative hypothesis for fibril sliding is the breaking of bonds between the hydroxyapatite particles and the matrix and a modification of the frictional stress between fibers (Tai et al. 2006). Lastly, microcracking provides a mechanism to relax plastic deformation; it is also a precursor to larger scale extrinsic toughening mechanisms. Examples of extrinsic toughening mechanisms include crack deflection along the osteon cement line and uncracked-ligament bridging. The anisotropic

fracture behavior of bone can be partially attributed to the orientation relationship of the crack plane and osteon cement lines. Longitudinal fracture is defined as crack propagation parallel to the longitudinal axis of the bone (i.e., parallel to osteons). In contrast, transverse fracture is defined as crack propagation perpendicular to the bone longitudinal axis (i.e., perpendicular to osteons). The cement line represents a mechanically weak layer along which cracks can more easily defect (Nalla et al. 2003; Norman and Wang 1997; Burr et al. 1988; Yeni and Norman 2000; Kruzic Nalla et al. 2005). As a result, fracture toughness is higher for transverse fracture and lower for longitudinal fracture (Behiri and Bonfield 1989; Feng et al. 2000; Lucksanasombool et al. 2001; Ritchie et al. 2006). Typically, notching of specimens is necessary to direct a crack to propagate perpendicular to the osteons (Nalla et al. 2003; Behiri and Bonfield 1989; Shannahan et al. 2015). However, once initiated, crack propagation paths are deviated by cement lines but continue to propagate transversely (Ritchie et al. 2006; Zimmermann et al. 2009).

In addition to the complex hierarchical structure of bone, specimens procured for study can be susceptible to additional confounding factors (e.g., age, weight, race, gender, metabolic disease) that present further challenges in refining understanding of fracture mechanics and toughening mechanism activity. In this study, healthy femoral bovine cortical bone dominated by a Haversian microstructure is selected for analysis to limit confounding factors, and heat treatments are implemented to provide a controlled approach for denaturing the collagen network. Bovine femur was selected for study due bovine bones having been demonstrated to be surrogate materials for human bone (e.g., Fletcher et al. 2018; Swartz et al. 1991). Opposed to using isotropic material assumptions when determining fracture parameters, such as when using ASTM standards E399, E1820, or C1421, an orthotropic material linear elastic fracture mechanics theory is adopted to provide critical mode-I and mode-II SIFs immediately before fracture initiation (i.e., fracture initiation toughness) that are determined from the near-crack tip displacement fields. Investigating the fracture behavior of cortical bone in healthy (control) and at increasing levels of collagen network degradation will provide an isolated assessment of the role that collagen-based intrinsic toughening mechanisms play under intermediate loading conditions.

2 Experimental methodology

2.1 Specimen preparation

Bovine cortical bone is used as a material model to assess the effect of collagen network quality on fracture behavior. All specimens used throughout the study were excised from the mid-diaphysis of a single healthy bovine femur procured from a local butcher shop. The bovine was feed lot raised to maturity and harvested at an age of approximately 18 months. To determine the predominant microstructure of the cortical bone present in the bovine femur mid-diaphysis, fluorescence imaging was used. Fluorescence imaging specimens were prepared by cutting and polishing a thin ($150 \mu m$) section of the femur which was then fixed using 10% neutral buffered formalin. The fixed section was stained in a solution consisting of 1 mg of fluorescein (Fluorescein isothiocyanate isomer I, Sigma Aldrich) in 100 mL of phosphate-buffered saline for two hours. After staining, the sample was dehydrated in 200 proof ethanol for 3 hours. The sample was then imaged using epifluorescence to visualize the cortical bone microstructure.

To prepare specimens for fracture testing, the femur mid-diaphysis was sectioned into quarters using a band saw with a diamond-coated blade. Further sectioning to nominal dimensions of 6.5 mm by 2.0 mm by 30 mm was performed using a low-speed diamond saw. The specimen's longitudinal axis is oriented to the longitudinal axis of the femur mid-diaphysis. Specimens were then polished to the final dimensions of 6 mm by 1.5 mm by 30 mm using 1200 grit silicon carbide paper. All preparation steps were performed under constant irrigation in phosphate-buffered saline (PBS). These specimen dimensions were selected to meet the ASTM E399, a commonly used standard in the bone mechanics community (e.g., Ritchie et al. 2008; Wang et al. 2002; Kuninori et al. 2009; Kikugawa and Asaka 2004; Poundarik et al. 2015). A notch was added to the midspan of the specimen length to a nominal depth of 2.5 mm using a 0.25 mm thick low-speed diamond saw blade. A custom-built reciprocating razor blade apparatus was used with a 1 μm diamond suspension as a lubricant to achieve a sharp notch tip with a root radius of 5 μm and a final depth of 3.0mm. A sharp notch tip is necessary to promote transverse fracture. Lastly, specimens were rinsed and ultrasonically cleaned in PBS to remove surface particulates. During all stages of prepa-

ration and storage, specimens were submerged in PBS to prevent bone dehydration.

To study the effect of collagen network denaturation on fracture behavior, specimens were separated into control and heat treatment groups. Collagen is a triple helix, which, when subjected to heat, denatures through unfolding. Non-mineralized collagen denatures at 60 °C, and mineralized collagen denatures at 150 °C (Bonar and Glimcher 1970; Danielsen 1987; Kronick and Cooke 1996; Notbohm et al. 1992). Heat treatment groups, consisting of at least 16 specimens each, were subjected to two hour treatments of 130 °C, 160 °C, and 190 °C, respectively. These three temperatures were selected to have a treatment group approaching the temperature when mineralized collagen denatures (130 °C), one just above when denaturing occurs (160 °C), and one well above when collagen denaturing occurs (190 °C). Heat treatments below 200 °C do not alter the mineral phase (Holden et al. 1995, ?). Therefore, the heat treatment groups only induce collagen network denaturation without altering the mineral phase. Furthermore, these heat treatment groups were selected as previous efforts involving micrographic analysis of heat-treated bone did not observe heat-treatment-induced microcracking (Wang et al. 2000). Microcracking is undesirable as it would result in a defect-riddled specimen. Once specimen heat treatments were completed, specimens were re-hydrated in PBS for 24 hours. The re-hydration step reverses bound water loss during heat treatment (Lucksanasombool et al. 2001; Nalla et al. 2006), and serves as an important step for preserving mechanical properties.

The total percentage of collagen denaturation achieved after heat treatment was determined using a trypsin-hydroxyproline assay protocol in accordance with that reported by Bank et al. (1997). After demineralization in 10% Ethylenediaminetetraacetic acid (EDTA), denatured collagen was digested in trypsin. Trypsin digests only the unfolded collagen filament. Then, the remaining collagen was acid-hydrolyzed in HCl to measure the quantity of intact collagen. Finally, using a microplate reader, absorbance was read at 561 nm and normalized to a standard hydroxyproline kit. The percentage of collagen digested is obtained by comparing the ratio of denatured collagen to intact collagen.

Prior to each drop tower experiment, the surface of each sample was lightly blotted with a Kim wipe to dry the surface. An Iwata Micron-B airbrush and Black India Ink were used to apply a uniformly random high contrast speckle pattern to the specimen surface to enable digital image correlation (DIC) analysis to measure in-plane displacements over the specimen surface and near the crack tip.

2.2 Drop tower experiments

Experiments were conducted in a symmetric three-point bend configuration on a custom-built, instrumented drop tower shown in Fig. 2. This drop tower has been used previously when reporting the mechanical behavior of human bone (e.g., Metcalf et al. 2021). The symmetric three-point bend configuration provides a mode-I loading condition (i.e., opening mode) to the specimen. The presence of any mode-II (i.e., sliding mode) loading or displacement fields is attributed to the orthotropic material symmetry and hierarchical microstructure of cortical bone. The support span used for all experiments was constant at 25.4 mm. A laser-based displacement sensor tracked the cross-head position over the duration of the experiment. After the specimen has fractured, two dampers arrest the cross-head.

The drop tower is capable of producing impact velocities matching those measured during fall events. Fall event impact velocities vary depending on fall direction, gait speed, and impact location (e.g., Smeesters et al. 2001; van den Kroonenberg et al. 1996; Pinilla et al. 1996. Previous studies have examined the impact force (i.e., Courtney et al. 1994; Robinovitch et al. 1991; Martel et al. 2018; Johnston et al. 2019) and impact velocity of the hip during a fall event Smeesters et al. 2001; van den Kroonenberg et al. 1996; Groen et al. 2008. Based on this previous work, an impact velocity of 1.6 m/s was used for all experiments which is in agreement with physiological fall velocities reported in literature which range between 1.2 and 4.8 m/s (e.g., Robinovitch et al. 1991). Impact velocities were confirmed from each experiment's the laser sensor time history. The selected impact velocity results in a nominal stress intensity factor rate of $\dot{K} = 1.5 \times 10^5 \, MPa \, m^{1/2}/s$, which was determined from the slope of the mode-I stress intensity factor vs. time history prior to fracture. The calculation of the mode-I stress intensity factor is provided in the following section.

A Shimadzu HPV-X2 high-speed camera equipped with an Infinity K2 long-distance microscope lens was

used to capture images of the deformation event and subsequent crack initiation and propagation. The HPV-X2 camera was triggered via a light gate consisting of a He-Ne laser and a photodetector (Electro-Optics Technology ET-2030). Uniform sample illumination was achieved using a pair of non-flickering constant-illumination LED arrays (GS Vitec Multiled QT) and two of Photogenic flash lamps (model PL2500DR) triggered by the laser light gate. During each experiment, the HPV-X2 captured 128 images at a frame rate of 500,000 fps.

Captured image sets were post-processed using DIC. The commercial software Vic2D-6, produced by Correlated Solutions, was used to obtain full-field in-plane displacement maps. Before each experiment, calibration images were captured to determine each image set's spatial resolution. The nominal spatial resolution of all image sets is 37.2 microns/pixel. Speckle patterns achieved using the patterning procedure described above were consistent. The following set of DIC analysis parameters was used for all image sets: subset size of 25 pixels, step size of 5 pixels, Gaussian subset weights, optimized 8-tap interpolation, and zero-normalized squared differences criterion.

3 Orthotropic material critical stress intensity factor determination

Stress intensity factor histories were determined using an over-deterministic linear least-squares approach. This method has been used in a broad range of investigations focusing on assessing the critical SIF of orthotropic materials (e.g., Shannahan et al. 2015; Sanford 1980; Kirugulige and Tippur 2009; Kirugulige et al. 2007; Yoneyama et al. 2006). The following analysis is limited to the case of a stationary crack. Thus, SIF histories were determined using the last image before crack initiation. Crack initiation was determined visually from captured image sets and confirmed from DIC displacement fields. The mode-I and mode-II SIFs calculated from the last frame of analysis are the critical stress intensity factors K_I^C and K_{II}^C (i.e., fracture initiation toughness).

When analyzing the area around the sharp notch (crack tip), the region from which displacement data is used must be carefully selected to ensure it matches the region of K-dominance (i.e., the region where linear elastic fracture mechanics is valid). Previous

works using displacement fields from high-speed photography and DIC have shown improved fits between asymptotic fields and experimentally resolved fields within an annulus around the crack tip spanning from -135 to $135°$ (Shannahan et al. 2015; Kirugulige et al. 2007). The inner radius of the annulus must be selected to avoid including both the plastic zone ahead of the crack tip and three-dimensional effects. As was shown by Tippur et al. (1991), if displacement data is only taken from the region of K-dominance, three-dimensional effects are minimized. Rosakis and Ravi-Chandar (1986) as well as Yang and Freund (1985) reported significant errors when determining SIFs when $r/b < 0.5$. For these reasons, the inner cut-off radius for the current investigation was selected to be $0.5\, r/b$. The annulus outer radius was selected to be $1.5\, r/b$ to avoid edge effects, shadowing, and image blurring caused by the loading nose extending in front of the image focal plane. These annulus bounds are similar to those used in previous studies of human cortical bone (e.g., Shannahan et al. 2015). The size of this annulus is indicated on the inset of Fig. 1.

Asymptotic crack tip displacement fields for mode-I and mode-II stress intensity factors, K_I and K_{II}, have been previously derived by Co Sih et al. (1965) for orthotropic materials, and take the from:

$$u_x = K_I\sqrt{\frac{2r}{\pi}}Re\left[\frac{1}{\mu_1-\mu_2}(p_1\mu_2 z_1 - p_2\mu_1 z_2)\right]$$
$$+ K_{II}\sqrt{\frac{2r}{\pi}}Re\left[\frac{1}{\mu_1-\mu_2}(p_1 z_1 - p_2 z_2)\right] \quad (1)$$

$$u_y = K_I\sqrt{\frac{2r}{\pi}}Re\left[\frac{1}{\mu_1-\mu_2}(q_1\mu_2 z_1 - q_2\mu_1 z_2)\right]$$
$$+ K_{II}\sqrt{\frac{2r}{\pi}}Re\left[\frac{1}{\mu_1-\mu_2}(q_1 z_1 - q_2 z_2)\right] \quad (2)$$

where, u_x and u_y are the displacement fields in the x (crack plane) and y (normal to the crack plane) directions, respectively.

The terms z_α, p_α, q_α, where $\alpha = 1, 2$ are position and material property dependent terms whose subscript values are determined by the two positive imaginary roots, μ_1 and μ_2 of the following 4th order polynomial given in Eq. 6.

$$z_\alpha = \sqrt{\cos\theta + \mu_\alpha \sin\theta} \quad (3)$$
$$p_\alpha = \mu_\alpha s_{11} + s_{12} - \mu_\alpha s_{16} \quad (4)$$

Fig. 1 Cortical bone specimen overview, **a** specimen extraction orientation **b** geometry, and **c** representative speckle pattern, coordinate system used during critical SIF determination, and region of K dominance
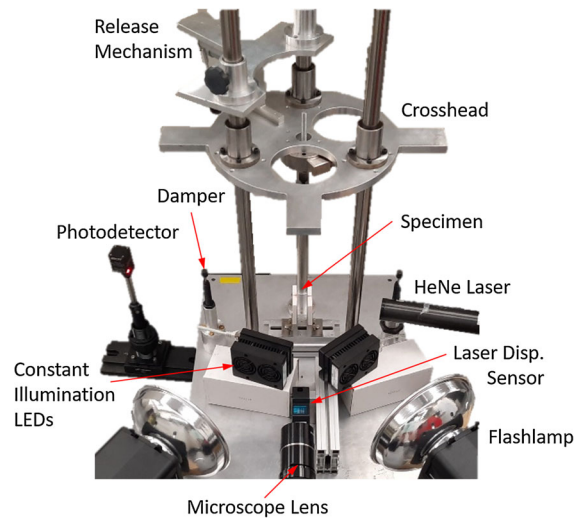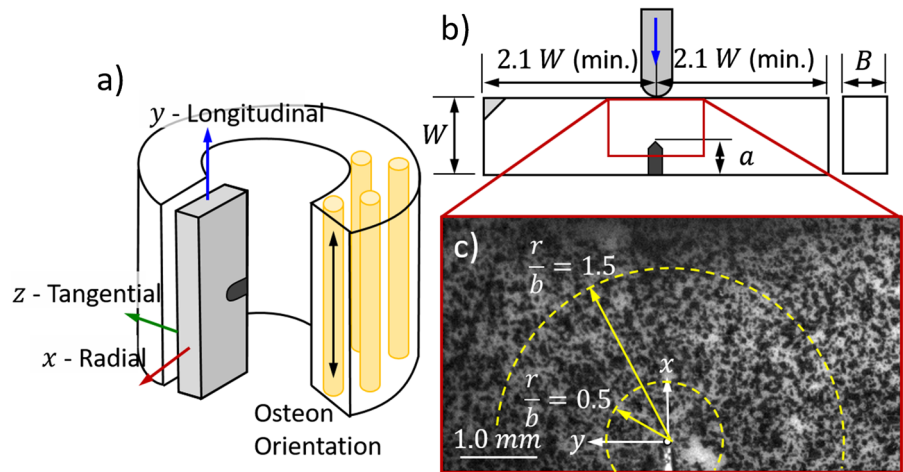
Fig. 2 The drop tower setup and primary components used to perform three-point bending loading configuration of single edge notched specimens at controlled impact velocities with high-speed imaging

$$q_\alpha = \mu_\alpha s_{12} + \frac{1}{\mu_\alpha} s_{22} - s_{26} \qquad (5)$$

$$\mu^4 s_{11} - 2s_{16}\mu^3 + (2s_{12} + s_{66})\mu^2 - 2s_{26}\mu + s_{22} = 0. \qquad (6)$$

The s_{ij} terms above are components of the orthotropic material compliance matrix written in Voigt notation. The values used to populate the compliance matrix were taken from the ultrasonic property measurements conducted by Van Buskirk et al. (1981) and are reported in Table 1. The use of ultrasound pulse transmission to measure elastic properties was favored over studies of

Table 1 Voigt notation compliance matrix values used

s_{11}	0.0859×10^{-9} Pa
s_{22}	0.0457×10^{-9} Pa
s_{12}	-0.0094×10^{-9} Pa
s_{16}	0
s_{26}	0
s_{66}	0.1587×10^{-9} Pa

bovine cortical bone that utilize quasi-static mechanical property testing due to the elastic constants measured dynamically being more closely aligned with the dynamic loading conditions of the drop tower experiments performed. In general, the elastic properties of bone are attributed to the mineral phase, while its plastic properties are conferred by collagen. As stated previously, the heat treatment temperatures and duration used will damage collagen through denaturation while the mineral phase is unaffected. Therefore, all specimens are assumed to have the same elastic properties regardless of heat treatment. One possible source of variability in the reported results is that the elastic constant values used in the anisotropic formulation are the average taken from multiple positions within a bovine femur. The natural variation of mechanical properties that occur over the mid-diaphysis could result in slight over/under predictions of the critical SIFs at fracture. Future studies will account for local property variation as a function of anterior vs. posterior position and height along the femur mid-diaphysis.

While the asymptotic displacement fields presented in Eqs. 1 and 2 are useful for the individual determination of K_I and K_{II}, Yoneyama et al. (2006), as well as Kirugulige and Tippur (2009) have shown the polar coordinate displacements, u_r and u_θ, are better suited for simultaneously solving for K_I and K_{II}. Furthermore, the use of polar coordinate displacements leads to the dominance of lower order terms. The Cartesian displacements are transformed using:

$$\begin{Bmatrix} u_r \\ u_\theta \end{Bmatrix} = \begin{bmatrix} \cos\theta & \sin\theta \\ -\sin\theta & \cos\theta \end{bmatrix} \begin{Bmatrix} u_x \\ u_y \end{Bmatrix} \tag{7}$$

Inserting Eqs. 1 and 2 into the the above transformation results in:

$$
\begin{aligned}
u_r = &\left(K_I \sqrt{\frac{2r}{\pi}} Re\left[\frac{1}{\mu_1 - \mu_2}(p_1\mu_2 z_1 - p_2\mu_1 z_2) \right] \ldots \right. \\
&+ \left. K_{II}\sqrt{\frac{2r}{\pi}} Re\left[\frac{1}{\mu_1 - \mu_2}(p_1 z_1 - p_2 z_2) \right] \right) \cos\theta \ldots \\
&+ \left(K_I \sqrt{\frac{2r}{\pi}} Re\left[\frac{1}{\mu_1 - \mu_2}(q_1\mu_2 z_1 - q_2\mu_1 z_2) \right] \ldots \right. \\
&+ \left. K_{II}\sqrt{\frac{2r}{\pi}} Re\left[\frac{1}{\mu_1 - \mu_2}(q_1 z_1 - q_2 z_2) \right] \right) \sin\theta \ldots \\
&+ R_x \cos\theta + R_y \sin\theta
\end{aligned}
\tag{8}
$$

where, R_x and R_y are rigid body translations. Eqs. 8 and 9 are for an individual point. They are rewritten in matrix form so that multiple points from the in-plane full-field displacement data obtained from DIC can be processed simultaneously. The polar displacement field u_r has displacement field components in the x and y directions, and thus only a single polar displacement is necessary to solve for both in-plane stress intensity factors, K_I and K_{II}. In order to solve for the desired values K_I, K_{II}, R_x and R_y a system of equations is constructed :

$$[\mathbf{U}] = [\mathbf{C}][\mathbf{X}] \tag{10}$$

The column vector [$\mathbf{U}$] contains the radial displacement of each DIC data point from 1 to n,

$$[\mathbf{U}] = \begin{bmatrix} u_r^1 \\ u_r^2 \\ \vdots \\ u_r^n \end{bmatrix} \tag{11}$$

The known terms of the radial displacement (Eq. 8) are placed into a matrix [$\mathbf{C}$]. To make the expression of matrix [C] more compact, the following $f_\alpha(r, \theta)$, $g_\alpha(r, \theta)$, $h_\alpha(r, \theta)$, and $k_\alpha(r, \theta)$ are assigned such that Eqs. 1 and 2 can be rewritten as:

$$u_x = K_I f_\alpha(r, \theta) + K_{II} g_\alpha(r, \theta) \tag{12}$$

$$u_y = K_I h_\alpha(r, \theta) + K_{II} k_\alpha(r, \theta) \tag{13}$$

$$[\mathbf{C}] = \begin{bmatrix} [f(r_1, \theta_1) + g(r_1, \theta_1)]\cos\theta_1 & [h(r_1, \theta_1) + k(r_1, \theta_1)]\sin\theta_1 & \cos\theta_1 & \sin\theta_1 \\ [f(r_2, \theta_2) + g(r_2, \theta_2)]\cos\theta_2 & [h(r_2, \theta_2) + k(r_2, \theta_2)]\sin\theta_2 & \cos\theta_2 & \sin\theta_2 \\ \cdots & \cdots & \cdots & \cdots \\ [f(r_n, \theta_n) + g(r_n, \theta_n)]\cos\theta_n & [h(r_n, \theta_n) + k(r_n, \theta_n)]\sin\theta_n & \cos\theta_n & \sin\theta_n \end{bmatrix} \tag{14}$$

$$
\begin{aligned}
u_\theta = &-\left(K_I \sqrt{\frac{2r}{\pi}} Re\left[\frac{1}{\mu_1 - \mu_2}(p_1\mu_2 z_1 - p_2\mu_1 z_2) \right] \ldots \right. \\
&+ \left. K_{II}\sqrt{\frac{2r}{\pi}} Re\left[\frac{1}{\mu_1 - \mu_2}(p_1 z_1 - p_2 z_2) \right] \right) \sin\theta \ldots \\
&+ \left(K_I \sqrt{\frac{2r}{\pi}} Re\left[\frac{1}{\mu_1 - \mu_2}(q_1\mu_2 z_1 - q_2\mu_1 z_2) \right] \ldots \right. \\
&+ \left. K_{II}\sqrt{\frac{2r}{\pi}} Re\left[\frac{1}{\mu_1 - \mu_2}(q_1 z_1 - q_2 z_2) \right] \right) \cos\theta \ldots \\
&- R_x \sin\theta + R_y \cos\theta
\end{aligned}
\tag{9}
$$

Lastly, the unknown in-plane stress intensity factors and rigid body translations to be solved for are placed into a column vector [$\mathbf{X}$].
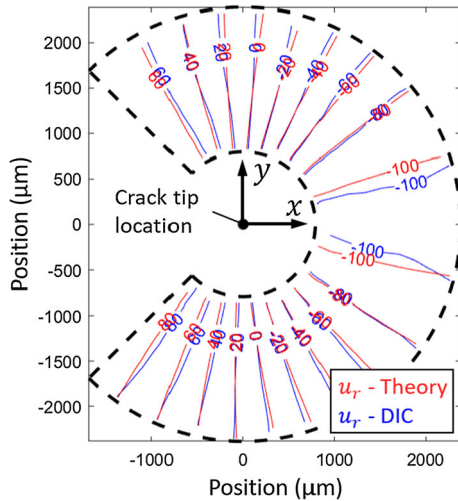
$$[\mathbf{X}] = \begin{bmatrix} K_I \\ K_{II} \\ R_x \\ R_y \end{bmatrix} \tag{15}$$

Using a least-squares fit, Eq. 10 is solved to determine the desired mode-I and mode-II stress intensity factors and in-plane translations:

$$[\mathbf{X}] = ([\mathbf{C}]^T[\mathbf{C}])^{-1}[\mathbf{C}]^T[\mathbf{U}]. \tag{16}$$

A comparison of the theoretical displacement field (generated using the critical mode-I and mode-II SIFs

Fig. 3 The representative correspondence between theoretical (red) and experimental radial (u_r) displacement fields (blue) in the annulus region used for analysis near the crack tip. Contour line amplitudes have units of micrometers

and rigid body rotations determined from Eq. 16) and the displacement field determined from DIC analysis, is shown in Fig. 3. These two fields should be in close correspondence to ensure meaningful solutions are obtained. In Fig. 3, the red contours represent the theoretical displacement field, and the blue contour represents the displacement field determined from DIC.

Many fracture resistance investigations have reported a single-valued representation of fracture toughness in the form of the strain-energy release rate (G). Physically, the strain-energy release rate is the change in potential energy per unit increase of crack surface area at fracture. Assuming linear-elasticity the single value energy release rate is related to the mode-I, mode-II, and mode-III stress-intensity factors through:

$$G = \frac{K_I^2}{E'} + \frac{K_{II}^2}{E'} + \frac{K_{III}^2}{2\mu}, \tag{17}$$

where, E' is the plane-strain elastic modulus ($E' = E/1 - \nu^2$, ν is Poisson's ratio) and μ is the shear modulus. The three point bending loading configuration utilized does not result in out-of-plane motion, and thus the mode-III (tearing) stress intensity factor $K_{III} = 0$ for all experiments. Thus, when calculating the single value strain-energy release rate only the mode-I and mode-II critical stress intensity factors are used. Recent work by, Nobakhti et al. (2017) characterized variations of the elastic modulus of bovine femurs using three-point bending and micro-computed tomography. The

average elastic modulus found over the mid-diaphysis using both techniques was $E = 19.43$ GPa. This modulus value and a Poisson's ratio of $\nu = 0.3$ are used when calculating strain-energy release rate.

4 Statistical analysis

Collagen denaturation, critical stress intensity factors, and energy release rate results were examined for statistical significance using a one-way ANOVA. Statistical significance among sample group means was identified when $p < 0.05$. If statistical significance among sample groups was observed, as will be shown to be the case when examining collagen denaturation as a function of heat treatment, a Tukey's honestly significant difference test was preformed to identify which group means are significantly different.

5 Results and discussion

5.1 Bovine cortical bone microstructure

A nominally representative fluorescence micrograph captured with a viewing direction parallel to the femur longitudinal direction is presented in Fig. 4. A Haversian cortical bone microstructure was observed evidenced by the presence of well-formed osteons ranging in diameter from 150 to 250 μm with centralized Haversian canals. The results shown here are in agreement with those obtained by Manilay et al. (2013) who found the lateral quadrant of cortical bone harvested from a mature 18 month old cow to present a well-developed Haversian microstructure. While Haversian cortical bone was predominatly observed among the micrographs collected, it should be expected that there could be regions of plexiform and plexiform combined with Haversian microstructures present within specimens. The amount of plexiform bone present is dependent on remodeling. Previous work of others (e.g., Lipson and Lawrence Katz 1984; Abdel-Wahab et al. 2011) has shown the microstructure of bovine bone to vary depending on the quadrant considered.

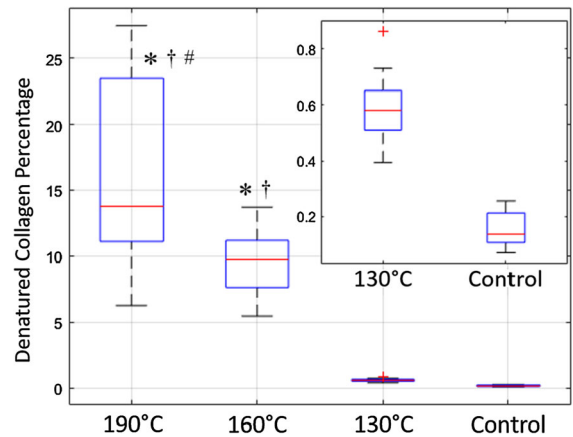### 5.2 Denatured collagen content quantification

The percentage of denatured collagen content of each specimen group was quantified using the trypsin-
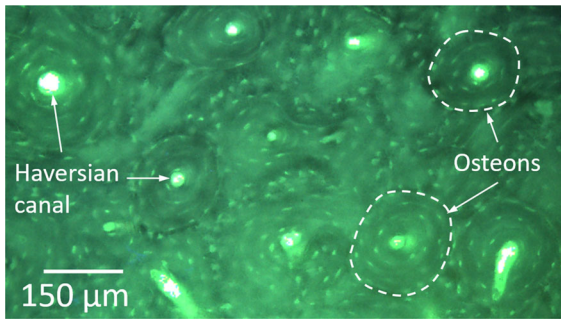
Fig. 4 A fluoresence micrograph showing an established Haversian microstructure. A select few osteons are outlined by dashed lines and Haversian canals are pointed out

Fig. 5 Denatured collagen content as a function of treatment condition. The top-right figure inset provides a zoomed in view of the collagen content of the 130 °C and control groups. *$P < 0.05$ vs. Control; † $P < 0.05$ vs. 130 °C; # $P < 0.05$ vs. 160 °C. The center mark (red) on each box indicates the median, bottom and top edges indicate the 25th and 75th percentile, whiskers extend to the most extreme data points, and those represented by a '+' indicate outliers

Table 2 Summary of Tukey's honestly significant difference test results (p values)

	HT 130°C	HT 160° C	HT 190° C
Control	0.995	2.01×10^{-4}	2.915×10^{-8}
HT 130° C	–	1.81×10^{-4}	1.78×10^{-8}
HT 160° C	–	–	0.013

hydroxyproline assay described previously. A total of 36 unique specimens were analyzed, eight from the control group, ten from the HT 130 °C group, nine from the HT 160 °C group, and nine from the HT 190 °C group. The differences in the denatured collagen percentage can be observed from the boxplot for each specimen condition in Fig. 5. On the box plots, the red line indicates median measurement. The upper bound and lower bound of the blue box indicate the 25th percentile and 75th percentile measurement, and the tails extending from the boxes present the complete measurement range. As would be expected, the control group had a near-zero amount of denatured collagen. Among the heat-treated groups, there is a positive correlation between temperature and denatured collagen network percentage. The average level of denatured collagen content and standard deviation for each treatment condition are: Control 0.15% ± 0.06%; 130 °C - 0.60% ± 0.14%; 160 °C - 9.5% ± 2.5%, 190 °C - 15.6% ± 7.6%. A statistically significant difference in the mean denatured collagen content was found among the four specimen conditions ($p = 0.019$). To identify which groups had statistically significant differences in denatured collagen content, comparisons of each were conducted using Tukey's honestly significant difference test, the results of which are summarized in Table 1.

A significant difference is present in Table 1 if $p < 0.05$. It was found that the denatured collagen network percentage present in the 190 °C and 160 °C groups were significantly different from the 130°C and control groups. There was no significant difference found between the HT 130 °C and control groups, indicating these two specimen conditions had similar

levels of denatured collagen (Table 2). These results indicate that at a temperature between 130 and 160 °C, significant collagen damage is accumulated for the heat treatment duration (2 h) examined, and the level of damage accumulated increases by a statistically significant amount. This occurrence was expected since mineralized collagen starts to denature at 150 °C. The presence of a small amount of denatured collagen in the 130 °C group should be expected as the trypsin-hydroxyproline assay does not distinguish between mineralized or non-mineralized collagen. With the heat treatments all exceeding the temperature at which non-mineralized collagen denatures (i.e., 60 °C), and with non-mineralized collagen comprising a small portion of the total collagen network in bone (e.g., 5–8% in humans Nimni et al. 1993), it would be expected that some level of denatured collagen would be present for any heat treatment exceeding 60 °C.

Table 3 Summary of fracture initiation toughness and energy release rate for each heat treatment group

Treatment	K_I^c - $MPa\sqrt{m}$		K_{II}^c - $MPa\sqrt{m}$		$G - kJ/m^2$	
	Mean	Std. Dev.	Mean	Std. Dev	Mean	Std. Dev.
190 °C	2.86	2.32	3.65	2.14	1.37	1.62
160 °C	3.54	2.47	5.37	2.37	2.36	1.63
130 °C	6.24	3.38	4.69	2.21	3.43	2.69
Control	4.58	3.81	4.70	2.77	3.12	3.10
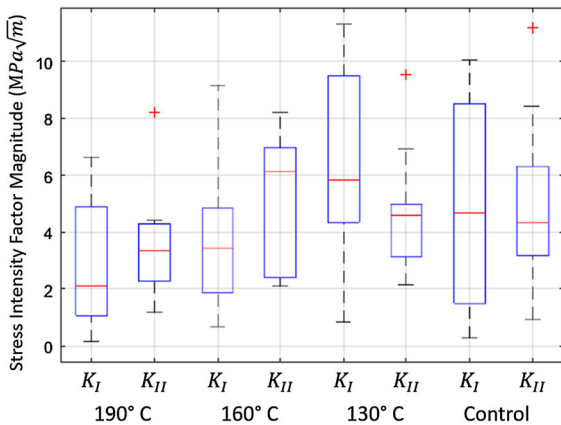
Fig. 6 An overview of the bovine cortical bone fracture initiation toughness organized with respect to heat treatment. Experiments were conducted at an impact velocity of 1.6 m/s, with a nominal stress intensity factor rate of $\dot{K} = 1.5 \times 10^5\ MPa\ m^{1/2}/s$
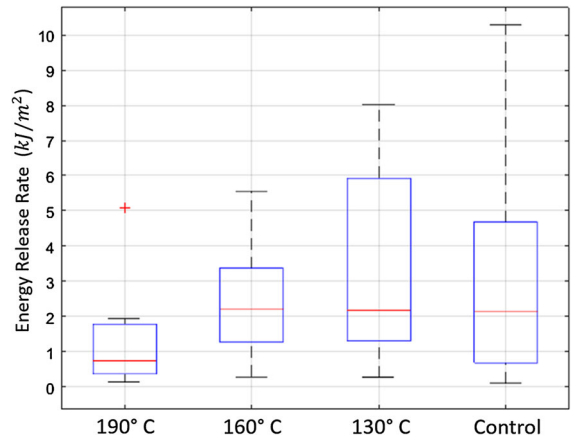
Fig. 7 An overview of the energy release rate for each heat treatment condition for a stress intensity factor rate of $\dot{K} = 1.5 \times 10^5 MPam^{1/2}/s$

5.3 Fracture initiation toughness and energy release rate

A summary of the fracture initiation toughness and energy release rate means and standard deviations for each heat treatment are reported in Table 3. Figures 6 and 7 present boxplots of the mode-I and mode-II fracture initiation toughness and energy release rates, respectively. As in Fig. 5, the center mark (red) on each box indicates the median, bottom and top edges indicate the 25th and 75th percentile, whiskers extend to the most extreme data points, and those represented by a '+' indicate outliers. The critical SIFs from each experiment are presented in Fig. 8 in the subsequent section.

5.4 Control group fracture initiation toughness

Despite a large number of studies having been conducted on the fracture behavior of bovine long bones

(e.g., Behiri and Bonfield 1989; Melvin 1973; Robertson et al. 1978; Bonfield and Datta 1976; Moyle and Gavens 1986; Behiri and Bonfield 1980; Norman et al. 1992; De Santis et al. 2000; Chen et al. 2008; Yan et al. 2006; Behiri and Bonfield 1984; Adharapurapu et al. 2006; Bonfield et al. 1978), comparing results obtained here to those in literature is challenging due to differences in loading rate, loading configuration, mode of fracture, specimen geometry, and the formulation used to determine fracture toughness. A common feature of the studies listed above is the determination of a single-value fracture toughness from the peak load at the onset of cracking under a prescribed loading mode (i.e., opening (mode-I), shearing (mode-II), or tearing (mode-III)). Fracture toughness values are then reported with respect to loading mode. This is in stark contrast to the approach used here, where fracture initiation toughness values are determined from observed in-plane displacement fields and the use of an orthotropic material formulation. Therefore, only
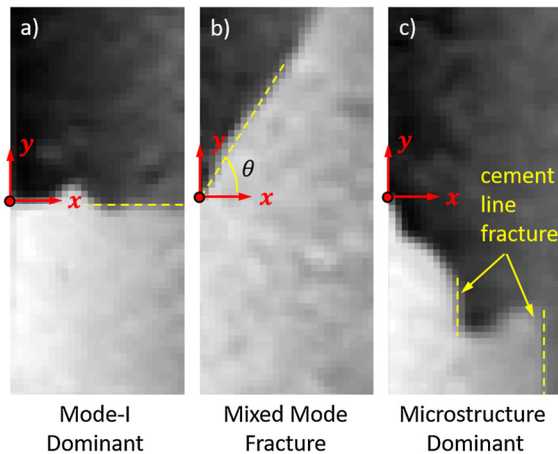
Fig. 8 An overview of the fracture types as determined from discontinuities of the displacement field in the y-direction (vertical direction in images shown). **a** Mode-I dominant fracture occurs along the original crack plane direction, **b** Mode-II dominant fracture where the crack path is inclined to the original crack plane with limited tortuosity, **c** Highly tortuous crack path demonstrating interactions with microstructure features such as cement lines

indirect comparisons can be made between the results reported in literature and those reported herein.

Robertson et al. (1978) used three-point bending to study transverse crack propagation on notched bovine femora specimens at quasi-static loading rates ranging from $7 \times 10^{-6} s^{-1}$ to $3 \times 10^{-2} s^{-1}$. They found a mode-I fracture toughness of 5.7 ± 1.4 MPa $m^{-1/2}$. Comparing their mode-I fracture toughness to the mode-I fracture initiation toughness measured herein, it is observed that the value of Robertson et al. is slightly above the control group mean but falls within the bounds of the standard deviation. Over the quasi-static strain rates examined in Ref. (Robertson et al. 1978), a positive but weak correlation with strain rate was reported indicating mild visco-elastic behavior. Others who have examined the rate sensitivity of the fracture behavior of cortical bone from humans (Shannahan et al. 2015) and bovines (Adharapurapu et al. 2006) from the quasi-static to dynamic regime have found cortical bone to behave in a brittle fashion at increasing stress intensity loading rates. The exact loading rate when the ductile fracture to brittle fracture transition occurs has yet to be comprehensively identified and is a worthy area of study.

Feng et al. (2000) assessed transverse fracture toughness under mode-I, mode-II, and mode-III load-

ing. They found mode-I fracture toughness to be roughly three times lower than mode-II or mode-III fracture toughness under quasi-static loading. To ensure transverse fracture, side grooves were added to specimens that suppressed the activation of extrinsic toughening mechanisms, mainly crack deflection, resulting in co-planar cracks. The forced co-planar crack path is unnatural and could be one governing cause for the significant difference between the fracture toughnesses observed of each loading mode. Side grooves were not utilized in the presented work as they are not compatible with two-dimensional DIC. The difference in the ratio of the critical mode-I SIF and the critical mode-II SIF found in the current work is approximately one for healthy bovine femoral cortical bone and is increased for denatured collagen network specimens.

5.5 Denatured collagen network fracture initiation toughness

A statistically significant difference in the fracture toughness values across the heat treatment conditions examined was not observed ($p = 0.24$). Due to a lack of statistical significance among the fracture initiation toughness values obtained, only trends can be identified. Following presents discussion of trends observed. The 130 °C heat treatment resulted in an increase of the critical mode-I SIF but did not affect the critical mode-II SIF. While the exact origins of the SIF increase are unknown, the work of Wang et al. (2000) also found an increase in the fracture properties of cortical bone at similar temperatures.

The 160 °C and 190 °C heat treatment groups exhibit a reduction in their fracture initiation toughness. This overall reduction points to collagen's role in serving as an intrinsic toughening mechanism for bovine cortical bone investigated and that collagen network damage induced via heat treatment denaturing has a limited affect on increased bone embrittlement under fall event loading rates. Additionally, for the 160 °C and 190 °C heat treatments the mean critical mode-II SIF is greater than the mean critical mode-I SIF. This occurs even though the symmetric three-point bending loading configuration places the sharp notch (i.e., crack) in a mode-I loading configuration. As stated previously, the presence of a mode-II response is caused by the orthotropic nature and hierarchical microstructure of
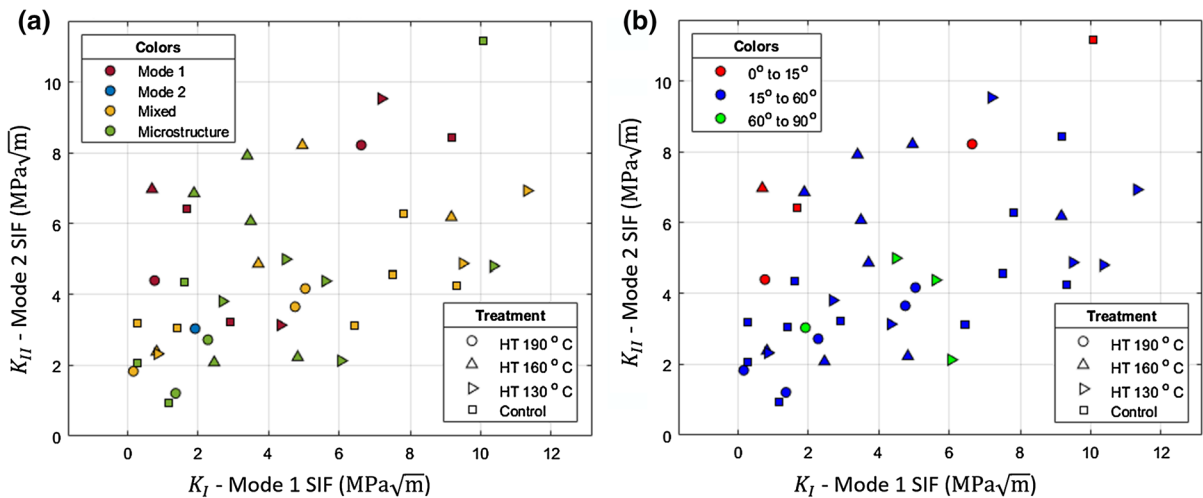
Fig. 9 Overview of **a** fracture type and **b** fracture initiation angle for each experiment

cortical bone. The overall reduction in the mode-I fracture initiation toughness, while the mode-II fracture initiation toughness remains less impacted, points to collagen primarily conferring mode-I fracture toughness in Haversian bovine cortical bone. In contrast, mode-II fracture toughness is conferred by alternative microstructural features. This observation agrees with known intrinsic toughening mechanisms, specifically collagen molecule stretching and unwinding and intermolecular sliding, whose operation depends on the tensile loading of collagen fibers.

5.6 Strain energy release rate

A statistically significant difference was not found within the strain energy release rate data ($p = 0.3$). Similar to the discussion of fracture initiation toughness, only trends in data can be discussed. From Table 3 it can be observed that there is a trend of the mean energy release rate decreasing for heat treatment temperatures above 160 °C, as would be expected with the trend of fracture initiation toughness decreasing with increasing heat treatment temperatures. The relative magnitude of the mean and median energy release rates for the control group representing healthy cortical bone, reported in Table 3 and Fig. 7 respectively, are in general agreement with the energy release rates reported for bovine cortical bone by Behiri and Bonfield (1984) ($2.9 kJ/m^2$), and the range given by Ritchie

et al. (2005) for generalized cortical bone (0.15–3.25 kJ/m^2).

6 Qualitative fracture analysis

Any alteration in the crack path trajectory or high levels of tortuosity gives insight into the role that extrinsic toughening mechanisms such as crack deflection play during the fracture processes. Qualitative observations of the path taken by the predominant crack, which caused the specimen to separate into two pieces, help to identify the dominant mode of fracture. Using the last image recorded from each experiment, the dominant crack trajectory can be determined from displacement field discontinuities (i.e., the jump from black to white in the vertical displacement fields shown in Fig. 8). An overview of three fracture types observed is shown in Fig. 8. Mode-I fracture paths were classified as generally flat, and with crack paths that start as co-planar to the notch plane or, after a short propagation distance, become co-planar. Mixed-mode cracks were generally flat, initiated at an inclined angle to the initial crack plane, and maintained that angle of inclination across the specimen. Microstructure dominant fracture is a further classification of the mixed-mode fracture where the crack initiated at an inclination angle, then deflected along a microstructural feature such as an osteon line during its transit across the specimen. Absent from Fig. 8 is Mode-II dominated fracture. Mode-II dominated fracture was classified as a crack that initiated

and propagated perpendicular to the initial notch plane. Mode-II dominated fracture was observed in a single experiment of the 41 conducted and therefore is not considered to be a predominant fracture mode for any of the specimen conditions examined. The initial crack angle was also determined from the vertical displacement discontinuity. Specimen crack angles were separated into three groups, 0 °-15 ° (quasi-mode-I), 15 °-60 ° (mixed mode) and 60 °–90 ° (quasi-mode-II).

The displacement field discontinuity provides an overview of the crack path that ultimately separates the specimen into two pieces but is unable to account for, (1) instances of microcracking or crack bifurcations occurring below the resolution limit of the camera or that of the subset size and step size used in DIC analysis, and (2) crack bridging processes occurring during crack growth. Therefore, the qualitative analysis is limited to providing insights into possible relationships between the critical stress intensity factors, the initial crack trajectory, and the prevalence of crack deflection of the propagating crack.

The dominant fracture type and initial fracture angle for each experiment conducted are presented in Fig. 9a and b, respectively. Mixed-mode and microstructure-dominated fracture were the two most prevalent fracture types observed in 32 of the 41 experiments conducted. This result is similar to what would be expected for notched specimens subjected to mode-I loading. The predominant initial crack propagation angle occurred between 15° and 60° from the initial crack plane. Both of these results are in agreement with the mixed-mode state at fracture initiation. In order for a deeper understanding of the interactions of the propagating crack stress field with microstructural features, an improved spatial resolution (i.e., greater magnification) is necessary. If improved resolutions can be achieved, a deeper understanding of the activity of extrinsic fracture mechanisms for dynamically propagating cracks in this orthotropic material could be obtained as currently, the rate sensitivity of intrinsic and extrinsic toughening mechanisms in bone are unknown. The similarities of the fracture paths observed at the selected physiological loading rate and those observed from quasi-static experiments point to extrinsic toughening mechanisms being contributing toughening mechanisms under fall events.

7 Summary

In this study, Haversian bovine cortical bone is used as a model material system to assess the effect of collagen network quality on elevated loading rate fracture initiation toughness. Collagen network quality was modified through heat treatments designed to denature mineralized collagen to increasing levels and was quantified using a trypsin-hydroxyproline assay. SIFs up to crack initiation were found using an over-deterministic least-squares analysis of displacement fields calculated using DIC analysis to measure mixed-mode fracture initiation toughness values. Trends were observed pointing to increasing levels of non-mineralized collagen denaturation resulting in a decrease in mode-I fracture initiation toughness. These results suggest, specifically for bovine cortical bone, collagen-based intrinsic toughening mechanisms provide mode-I fracture toughening under elevated loading conditions. At the same time, mode-II fracture toughness is conferred by higher lengthscale microstructure features as it was less affected by the levels collagen denaturation achieved via the heat treatments investigated. Strain energy release rates also exhibited a trend, demonstrating a reduction as denatured collagen content increased. Two dominant fracture types were observed, namely mixed-mode fracture and micro-structurally dominated fracture along cement lines, regardless of the specimen treatment condition.

References

Adel AA-W, Khurshid A, Vadim VS (2011) Analysis of anisotropic viscoelastoplastic properties of cortical bone tissues. J Mech Behav Biomed Mater 4(5):807–820

Ares JR, Ravi-Chandar K (1986) On crack-tip stress state: an experimental evaluation of three-dimensional effects. Int J Solids Struct 22(2):121–134

Atharva AP, Wu P-C, Zafer E, Grazyna ES, Ani U, Mishaela R, Deepak V (2015) A direct role of collagen glycation in bone fracture. J Mech Behav Biomed Mater 52:120–130

Behiri JC, Bonfield W (1980) Crack velocity dependence of longitudinal fracture in bone. J Mater Sci 15(7):1841–1849

Behiri JC, Bonfield W (1984) Fracture mechanics of bone—the effects of density, specimen thickness and crack velocity on longitudinal fracture. J Biomech 17(1):25–34

Behiri JC, Bonfield W (1989) Orientation dependence of the fracture mechanics of cortical bone. J Biomech 22(8–9):863–872

Bonfield W, Datta PK (1976) Fracture toughness of compact bone. J Biomech 9(3):131–134

Bonfield W, Grynpas MD, Young RJ (1978) Crack velocity and the fracture of bone. J Biomech 11(10–12):473–479

Brian SN, Sol B, Wendelin P, Marcel EN (1993) Changes in the ratio of non-calcified collagen to calcified collagen in human vertebrae with advancing age. Connect Tissue Res 29(2):133–140

Cecile S, Wilson CH, Thomas AM (2001) Disturbance type and gait speed affect fall direction and impact location. J Biomech 34(3):309–317

Chen PY, Sheppard FA, Curiel JM, McKittrick J (2008) Fracture mechanisms of bone: a comparative study between antler and bovine femur. MRS online proceedings library archive, 1132

Christian DC (1987) Thermal stability of human-fibroblast-collagenase-cleavage products of type-i and type-iii collagens. Biochem J 247(3):725–729

Claire A, Meghan S, Eric S, James LG, Kimber LS, Lionel NM, Bernd G, Ann VS, Robert OR, Tamara NA et al (2018) Contributions of material properties and structure to increased bone fragility for a given bone mass in the ucd-t2dm rat model of type 2 diabetes. J Bone Mineral Res 33(6):1066–1075

Co Sih G, Paris PC, Irwin GR (1965) On cracks in rectilinearly anisotropic bodies. Int J Fract Mech 1(3):189–203

Courtney AC, Wachtel EF, Myers ER, Hayes WC (1994) Effects of loading rate on strength of the proximal femur. Calcif Tissue Int 55(1):53–58

Currey JD (2003) The many adaptations of bone. J Biomech 36(10):1487–1495

Daniel RM, Iris CL, Steven PP, Andrew CL (2018) The influence of muscle activation on impact dynamics during lateral falls on the hip. J Biomech 66:111–118

David BB, Mitchell BS, Richard GF (1988) Composition of the cement line and its possible mechanical role as a local interface in human compact bone. J Biomech 21(11):939–945

De Santis R, Anderson P, Tanner KE, Ambrosio L, Nicolais L, Bonfield W, Davis GR (2000) Bone fracture analysis on the short rod chevron-notch specimens using the X-ray computer micro-tomography. J Mater Sci: Mater Med 11(10):629–636

Elizabeth AZ, Maximilien EL, Holly DB, Robert OR (2009) Mixed-mode fracture of human cortical bone. Biomaterials 30(29):5877–5884

Elizabeth AZ, Bernd G, Eric S, Björn B, Robert OR (2014) Fracture resistance of human cortical bone across multiple length-scales at physiological strain rates. Biomaterials 35(21):5472–5481

Fletcher JWA, Sean Williams MR, Whitehouse HS Gill, Preatoni Ezio (2018) Juvenile bovine bone is an appropriate surrogate for normal and reduced density human bone in biomechanical testing: a validation study. Sci Rep 8(1):1–9

Georg EF, Tue H, Johannes HK, James CW, Henrik B, Leonid P, Jacqueline AC, Geraldo AGC, Galen DS, Daniel EM et al (2005) Sacrificial bonds and hidden length dissipate energy as mineralized fibrils separate during bone fracture. Nat Mater 4(8):612–616

Groen BE, Weerdesteyn V, Jaak D (2008) The relation between hip impact velocity and hip impact force differs between sideways fall techniques. J Electromyogr Kinesiol 18(2):228–234

Gwendolen CR, John DC (2000) The effects of damage and microcracking on the impact strength of bone. J Biomech 33(3):337–343

Hans Oxlund M, Gitte Ørtoft B, Andreassen TT (1995) Reduced concentrations of collagen cross-links are associated with reduced strength of bone. Bone 17(4):S365–S371

Hareesh VT, Sridhar K, Ares JR (1991) Optical mapping of crack tip deformations using the methods of transmission and reflection coherent gradient sensing: a study of crack tip k-dominance. Int J Fract 52(2):91–117

Hisao K, Takashi A (2004) Effect of long-term formalin preservation on bending properties and fracture toughness of bovine compact bone. Mater Trans 45(10):3060–3064

Holden JL, Clement JG, Phakey PP (1995) Age and temperature related changes to the ultrastructure and composition of human bone mineral. J Bone Mineral Res 10(9):1400–1409

Holden JL, Phakey PP, Clement JG (1995) Scanning electron microscope observations of heat-treated human bone. Forensic Sci Int 74(1–2):29–45

Holger N, Stephan M, Michael B, Chunlin Y, Hartwig L, Boris B, Peter KM (1992) Comparative study on the thermostability of collagen i of skin and bone: influence of posttranslational hydroxylation of prolyl and lysyl residues. J Protein Chem 11(6):635–643

James DJ, Chantal EK, Joel LL, Saija AK (2019) A single-spring model predicts the majority of variance in impact force during a fall onto the outstretched hand. J Biomech. 90:149–152

Jiahau Y, Kari BC, John JM, Roger LR (2006) Fracture toughness of manatee rib and bovine Femur using a Chevron-notched beam test. J Biomech 39(6):1066–1074

John DC (2006) Bones: structure and mechanics. Princeton University Press, Princeton

Karl JJ, Steven AG, Janet LK, Mitchell BS, Jeffrey B (1996) Type-i collagen mutation compromises the post-yield behavior of mov13 long bone. J Orthop Res 14(3):493–499

Karl JJ, Mitchell BS, Janet LK, Robert WG, Jeffrey B, Steven AG (1997) Type i collagen mutation alters the strength and

fatigue behavior of mov13 cortical tissue. J Biomech 30(11–12):1141–1147

Kirugulige MS, Tippur HV (2009) Measurement of fracture parameters for a mixed-mode crack driven by stress waves using image correlation technique and high-speed digital photography. Strain 45(2):108–122

Kuangshin T, Franz-Josef U, Christine O (2006) Nanogranular origins of the strength of bone. Nano Lett 6(11):2520–2525

Laurence CB, Melvin JG (1970) Thermal denaturation of mineralized and demineralized bone collagens. J Ultrastruct Res 32(5–6):545–557

Liu D, Wagner HD, Weiner S (2000) Bending and fracture of compact circumferential and osteonal lamellar bone of the baboon tibia. J Mater Sci Mater Med 11(1):49–60

Logan S, Tusit W, Allan G, Brett S, Leslie L (2015) Rate-dependent fracture modes in human femoral cortical bone. Int J Fract 194(2):81–92

Lucksanasomboool P, Higgs WAJ, Higgs RJED, Swain MV (2001) Fracture toughness of bovine bone: influence of orientation and storage media. Biomaterials 22(23):3127–3132

Madhu SK, Hareesh VT, Thomas SD (2007) Measurement of transient deformations using digital image correlation method and high-speed photography: application to dynamic fracture. Appl Opt 46(22):5083–5096

Margel RD, David R, Craig RB (1978) Fracture toughness, critical crack length and plastic zone size in bone. J Biomech 11(8–9):359–364

Maria LH, Lynne SB (2007) Differentiating human bone from animal bone: a review of histological methods. J Forensic Sci 52(2):249–263

Markus JB (2007) Molecular nanomechanics of nascent bone: fibrillar toughening by mineralization. Nanotechnology 18(29):295102

Masahiro K, Hisao K, Takashi A, Hirakazu K (2009) Effect of different preservative methods on fracture behavior of bovine cortical bone. Mater Trans 50:305–412

Matthew JS, Gibson LJ (1997) Modeling the mechanical behavior of vertebral trabecular bone: effects of age-related changes in microstructure. Bone 21(2):191–199

Maximilien EL, Markus JB, Robert OR (2010) On the mechanistic origins of toughness in bone. Ann Rev Mater Res 40:25–53

Melvin JW (1973) Crack propagation in bone. In: Abstract of ASME 1973 biomechanical symposium, pp. 87–88

Michael S (2001) Paleohistopathology of bone: a new approach to the study of ancient diseases. Am J Phys Anthropol 116(S33):106–147

Michael C, Johnson S (2016) Machining characteristics of the Haversian and plexiform components of bovine cortical bone. J Mech Behav Biomed Mater 60:525–534

Moyle DD, Gavens AJ (1986) Fracture properties of bovine tibial bone. J Biomech 19(11):919–927

Nalla RK, Kinney JK, Tomsia AP, Ritchie RO (2003) Mechanistic fracture criteria for the failure of human cortical bone. Nat Mater 2(3):164–168

Nalla RK, Kruzic JJ, Kinney JH, Ritchie RO (2004) Effect of aging on the toughness of human cortical bone: evaluation by r-curves. Bone 35(6):1240–1246

Nalla RK, Jamie JK, John HK, Robert OR (2005) Mechanistic aspects of fracture and r-curve behavior in human cortical bone. Biomaterials 26(2):217–231

Nalla RK, Kinney JK, Tomsia AP, Ritchie RO (2006) Role of alcohol in the fracture resistance of teeth. J Dent Res 85(11):1022–1026

Paul LK, Peter C (1996) Thermal stabilization of collagen fibers by calcification. Connect Tissue Res 33(4):275–282

Peter Z, Ulrich H, John DC (2008) Microcracking damage and the fracture process in relation to strain rate in human cortical bone tensile failure. J Biomech 41(14):2932–2939

Pinilla TP, Boardman KC, Bouxsein ML, Myers ER, Hayes WC (1996) Impact direction from a fall influences the failure load of the proximal femur as much as age-related bone loss. Calcified tissue international 58(4):231–235

Raghavendra RA, Fengchun J, Kenneth SV (2006) Dynamic fracture of bovine bone. Mater Sci Eng C 26(8):1325–1332

Ritchie RO, Koester KJ, Ionova S, Yao Wei, Lane Nancy E, Ager Iii JW (2008) Measurement of the toughness of bone: a tutorial with special reference to small animal studies. Bone 43(5):798–812

Robb MK, Fengchun J, Kenneth SV (2011) Effects of age and loading rate on equine cortical bone failure. J Mech Behav Biomed Mater 4(1):57–75

Robert JS (1980) Application of the least-squares method to photoelastic analysis. Exp Mech 20(6):192–197

Robert OR, John HK, Jamie JK, Ravi KN (2005) A fracture mechanics and mechanistic approach to the failure of cortical bone. Fatigue Fract Eng Mater Struct 28(4):345–371

Robert OR, Kinney JH, Kruzic JJ, Nalla RK (2006) Cortical bone fracture. Wiley encyclopedia of biomedical engineering. Wiley, New York

Robert MM, Jessica MC, Brittany C (2021) High-rate anisotropic properties in human infant parietal and occipital bone. J Biomech Eng 143(6):061010

Robinovitch SN, Wilson CH, McMahon TA (1991) Prediction of femoral impact forces in falls on the hip. J Biomech Eng 113:366–374

Ruud AB, Marianne K, Bob B, Reinout S, Alice M, Floris PJGL, Johan MTK (1997) A simplified measurement of degraded collagen in tissues: application in healthy, fibrillated and osteoarthritic cartilage. Matrix Biol 16(5):233–243

Sabah N, Orestis LK, Nizar Z, Georges L, Philipp JT (2017) Elastic modulus varies along the bovine femur. J Mech Behav Biomed Mater. 71:279–285

Sanborn B, Gunnarsson CA, Foster M, Weerasooriya T (2016) Quantitative visualization of human cortical bone mechanical response: studies on the anisotropic compressive response and fracture behavior as a function of loading rate. Exp Mech 56(1):81–95

Sidney L, Douglas H, Elizabeth P, Herbert AM (1994) Comparison of dosage-dependent effects of β-aminopropionitrile, sodium fluoride, and hydrocortisone on selected physical properties of cortical bone. J Bone Mineral Res 9(9):1377–1389

Sommerfeldt D, Rubin C (2001) Biology of bone and how it orchestrates the form and function of the skeleton. Eur Spine J 10(2):S86–S95

Steve W, Wagner HD (1998) The material bone: structure–mechanical function relations. Ann Rev Mater Sci 28(1):271–298

Steve W, Wolfie T, Wagner HD (1999) Lamellar bone: structure–function relations. J Struct Biol 126(3):241–255

Susan FL, Katz JL (1984) The relationship between elastic properties and microstructure of bovine cortical bone. J Biomech 17(4):231–240

Swartz DE, Wittenberg RH, Shea M, White AA III, Hayes WC (1991) Physical and mechanical properties of calf lumbosacral trabecular bone. J Biomech 24(11):1059–1068

Tanabe Y, Tanner KE, Bonfield W (1998) Effect of loading rate on fracture toughness of bovine cortical bone. J Biomech 1001(31):121

Timothy LN, Wang Z (1997) Microdamage of human cortical bone: incidence and morphology in long bones. Bone 20(4):375–379

Timothy LN, Vashishth D, Burr DB (1992) Effect of groove on bone fracture toughness. J Biomech 25(12):1489–1492

Todoh M, Tadano S, Imari Y (2009) Effect of heat denaturation of collagen matrix on bone strength. 13th international conference on biomedical engineering. Springer, Berlin, pp 2034–2037

Ulrich H, Peter Z, Rebecca S, John DC, David H (2008) The effect of strain rate on the mechanical properties of human cortical bone. J Biomech Eng 130:11011

Van Buskirk WC, Cowin SC, Ward Ro N (1981) Ultrasonic measurement of orthotropic elastic constants of bovine femoral bone. J Biomech Eng 103:67–72

van den Kroonenberg Aya J, Wilson CH, Thomas AM (1996) Hip impact velocities and body configurations for voluntary falls from standing height. J Biomech 29(6):807–811

Wang X, Shen X, Li X, Mauli Agrawal C (2002) Age-related changes in the collagen network and toughness of bone. Bone 31(1):1–7

Wei Y, Freund LB (1985) Transverse shear effects for through-cracks in an elastic plate. Int J Solids Struct 21(9):977–994

Xiaodu W, Ruud AB, Johan MT, Gene BH, Kyriacos AA, Agrawal CM (2000) Effect of collagen denaturation on the toughness of bone. Clin Orthop Relat Res 371:228–239

Xuedong Z, Jinling G, Yizhou N, Zherui G, Nesredin K, Ben C, Tao S, Kamel F, Xianghui X, Weinong WC (2019) Real-time visualization of dynamic fractures in porcine bones and the loading-rate effect on their fracture toughness. J Mech Phys Solids 131:358–371

Yener NY, Timothy LN (2000) Calculation of porosity and osteonal cement line effects on the effective fracture toughness of cortical bone in longitudinal crack growth. J Biomed Mater Res 51(3):504–509

Yeni YN, Timothy NL (2000) Fracture toughness of human femoral neck: effect of microstructure, composition, and age. Bone 26(5):499–504

Yoneyama S, Morimoto Y, Takashi M (2006) Automatic evaluation of mixed-mode stress intensity factors utilizing digital image correlation. Strain 42(1):21–29

Zherrina M, Ekaterina N, Ernest S, Joanna M (2013) A comparative study of young and mature bovine cortical bone. Acta Biomater 9(2):5280–5288

Zude F, Jae R, Seung H, Israel Z (2000) Orientation and loading condition dependence of fracture toughness in cortical bone. Mater Sci Eng C 11(1):41–46